Detailed Tuning of Structure and Intramolecular Communication Are Dispensable for Processive Motion of Myosin VI

Mary Williard Elting,[†‡] Zev Bryant,[§] Jung-Chi Liao,[§] and James A. Spudich[†*]
[†]Department of Biochemistry, [‡]Department of Applied Physics, and [§]Department of Bioengineering, Stanford University, Stanford, California

ABSTRACT Dimeric myosin VI moves processively hand-over-hand along actin filaments. We have characterized the mechanism of this processive motion by measuring the impact of structural and chemical perturbations on single-molecule processivity. Processivity is maintained despite major alterations in lever arm structure, including replacement of light chain binding regions and elimination of the medial tail. We present kinetic models that can explain the ATP concentration-dependent processivities of myosin VI constructs containing either native or artificial lever arms. We conclude that detailed tuning of structure and intramolecular communication are dispensable for processive motion, and further show theoretically that one proposed type of nucleotide gating can be detrimental rather than beneficial for myosin processivity.

INTRODUCTION

Myosin VI has cellular roles ranging from transporter to anchor in vivo (1,2). In vitro, it is processive (defined as taking multiple steps along an actin filament before detaching) and shares features with processive (+)-end directed myosins, including a hand-over-hand mechanism (3), strides that approximately span the pseudorepeat of the actin helix (4), and intramolecular gating (5). However, the detailed mechanisms of myosin VI processivity might be expected to diverge from other myosins due to a number of unique structural and functional characteristics: it achieves (−)-end-directed motion due to a unique insert following the catalytic domain that redirects its lever arm in the opposite direction from other known myosins (6–8), and it has an unusual lever arm structure with two light-chain-binding domains (9) followed by a sequence that forms an extended single α-helix as an isolated fragment (10).

Myosin VI stepping is gated (5): communication between the two heads keeps their kinetic cycles out of phase. This communication is thought to occur via tension transmitted through the lever arms that connect the heads, altering the kinetics in such a way that front head release is prevented (11,12). Previous work suggests two possible mechanisms producing gating in myosin VI. The rate of ADP release may be reduced in the front head when both heads are bound to actin (5), as is known to occur in myosin V (13). Reported reductions in this rate range from two- (14) to at least 10-fold (15) for myosin VI.

Alternatively, there is evidence of a reduced rate of ATP binding to the front head (16). Either mechanism is capable of preventing front head release, because the myosin VI head remains strongly attached to the actin filament in both the ADP-bound and the nucleotide-free state. Although it has been suggested that myosin VI must have a different gating mechanism than myosin V because of its reverse directionality (17), ADP release could be affected by multiple structural distortions, and either gating mechanism seems physically plausible. The properties of the lever arm and tail structure of myosin VI, and of other molecular motors, have been proposed to be important for successful intramolecular tension sensing, and therefore for gating and processivity (15,18,19).

In this work, we probe the structures and mechanisms underlying myosin VI processivity. Mechanistic models of myosins (15,20–25) and of kinesin (26–29) have been tested by engineering changes into these molecular motors and examining whether their behaviors respond predictably. We previously incorporated an artificial lever arm into a myosin VI dimer and showed that the chimera remains processive (21). Here, we examine the same chimera in detail to probe the effects of the structural changes on processivity. We use kinetic modeling, fit to our processivity data for constructs with native or artificial lever arms, to examine the relevance of gating to processivity.

We present models that explain our observed processivities over a wide range of conditions, and show theoretically that gating of ADP release yields only modest improvements in processivity, while gating of ATP binding actually decreases processivity at physiological ATP concentrations. Processivity seems to be a robust characteristic of dimeric molecular motors with high duty ratios even in the absence of gating. This idea is underscored by the processive activity of additional chimeric constructs in which we have incorporated increasingly dramatic changes in lever arm structure.

Submitted June 22, 2010, and accepted for publication November 16, 2010.

*Correspondence: jspudich@stanford.edu

Jung-Chi Liao's present address is Department of Mechanical Engineering, Columbia University, New York, NY.

Editor: Claudia Veigel.

0006-3495/11/01/0430/10 $2.00

doi: 10.1016/j.bpj.2010.11.045

MATERIALS AND METHODS

Protein expression and purification

Proteins were expressed as described (7,21). Briefly, myosin VI or chimeras were cloned into pBiEx-1 (see also the Supporting Material) and transfected into SF9 cells, Flag affinity purified, and labeled with TMR-HaloTag ligand (Promega, Madison, WI).

Single-molecule TIRF microscopy

Single-molecule TIRF microscopy was performed as described (21) (see also the Supporting Material). Briefly, actin was attached to coverslip surfaces using heavy meromyosin (HMM) prepared from rabbit skeletal muscle and treated with *n*-ethyl maleimide (NEM) to inactivate it so that it would bind actin but not detach. After rinsing out unattached actin filaments, motor was flowed into the chamber in assay buffer including ATP and reagents for ATP regeneration and oxygen scavenging. Additionally, $MgCl_2$ was added at a concentration that varied with ATP concentration and was chosen to result in 2 mM free Mg^{2+} (or other Mg^{2+} concentration as noted). Expected free Mg^{2+} concentrations were calculated using MAXCHELATOR (http://maxchelator.stanford.edu). A 532-nm laser was used for excitation, and its power was lowered to prevent misinterpreting photobleaching as run termination when measuring processivity. Images were analyzed by single-molecule tracking (30).

Stride size and dwell-time measurement

One-dimensional distance versus time traces created from two-dimensional tracking data and steps were chosen using a step-picking algorithm based on Kerssemakers et al. (31) (see also the Supporting Material). We used this algorithm to generate fits with varying numbers of steps, but picked the number of steps in each run by eye.

Run-length and velocity measurements

For details, see the Supporting Material. In brief, to ensure unbiased run selection, custom software was used to create a kymograph for each actin filament (Fig. S1). Runs were selected from these kymographs. The expected run-length, corrected for premature terminations of runs that ended at the end of a filament, was calculated using the Kaplan-Meier survivor function, a maximum likelihood estimator of the mean (32,33). The error bars are the error on the mean estimate from the Kaplan-Meier survivor function (32). The average velocity was calculated using a bootstrap fit of the slope of a plot of the average distance traveled for every δ-time for all runs (Fig. S2). The mean and standard deviation of 50 bootstraps were used as the velocity and error estimate for each data set.

Run-length modeling

A simplified model of the kinetic cycle of myosin VI was created with only three states for each head: bound to actin and ADP, bound to actin but not ADP, and bound to ATP and released from actin. Some states of a more complete kinetic cycle (see later in Fig. 2 *a*) were omitted (and assumed to be rarely visited) or were collapsed into one of the three remaining states. Transfers between states were approximated as irreversible (see later in Fig. 2 *b*). A branched kinetic model was created that included all combinations of these three states in each of the two heads (see later in Fig. 2 *c*). This model included a total of five parameters: two ADP release rates corresponding to the front and rear heads, two effective ATP binding rates corresponding to the front and rear heads, and the rebinding rate of the free head.

The relative rates of ADP release from the front and rear heads or of ATP binding to the front and rear heads were not allowed to vary independently, but were set at a fixed ratio depending on the gating mechanism used for the fit, as described in the text. An additional parameter was added to compensate for premature run termination due to actin attachment or defects in the actin filament, since we found that actin attachment mechanisms affect processivity (see below). Run-lengths and durations as a function of ATP concentration were analytically calculated by summing over all possible paths to run termination (see derivation in the Note in the Supporting Material). This modeling was verified by Monte Carlo simulations of the same process, which agreed well with the analytic version (Fig. S3).

To fit parameters to the model, the apparent ATP binding rate and ADP release rates were fit in a least-squares manner to the velocity data. (Note that although these velocity plots resemble Michaelis-Menten plots, they are not fit to simple Michaelis-Menten kinetics. Instead, the data are fit directly to velocities calculated using the comprehensive kinetic model.) These rates were fixed and the rebinding rate and actin defect parameters were fit using the run-length data. Alternating fits were then performed of the velocity and run-length data, as described, until all four rates converged. Error estimates for the fits were generated by using the standard deviation of the parameters from a parametric bootstrap comprising 1000 randomly generated data sets based on the measured mean and error for each run-length or velocity data point. (See Methods in the Supporting Material for more details.)

RESULTS

The behavior of dimeric myosin VI and a chimeric construct are similar

Gating is thought to arise from tension transmitted through the lever arm. To assess the impact on processivity of altering the lever am structure, we conducted a detailed characterization of an engineered processive myosin we previously constructed (21). In $M6DI_{816}$-2R~MT-GCN4, the IQ and proximal tail domains were removed and replaced with an artificial lever arm (two spectrin repeats from α-actinin, abbreviated as 2R (20)) fused after the distal portion of the unique insert, followed by a $(GSG)_3$ flexible-linker swivel (~), and the medial tail (MT), with GCN4 used to ensure dimerization. We compared this to our myosin VI control dimer (4), M6-GCN4, which contains native sequence through the medial tail, followed by GCN4 for dimerization (Fig. 1 and Movie S1 and Movie S2 in the Supporting Material). Using single molecule total internal reflection fluorescence (TIRF) microscopy, we found that the stride size distributions for $M6DI_{816}$-2R~MT-GCN4 and M6-GCN4 are similar (Fig. 1, *c* and *d*), as we showed previously under different actin conditions (21). Here, we show that the two constructs also have similar dwell-time distributions (Fig. 1 *e*). We then compared them to test for effects of the artificial lever arm on gating and processivity.

Modeling effects of gating on processivity

Kinetic models of processive motion can be tested by measuring run-length as a function of nucleotide conditions (34). To generate predictions of the effects of gating mechanisms, we constructed models of myosin VI processivity.

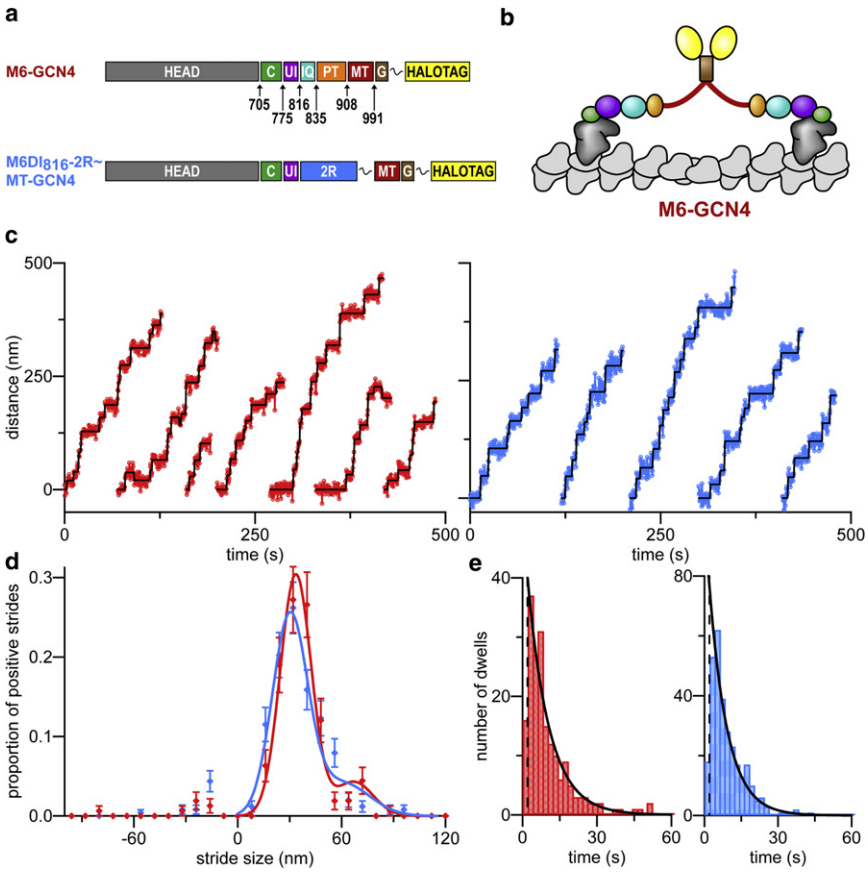

FIGURE 1 Single molecule stepping results for M6-GCN4 and M6DI$_{816}$-2R~MT-GCN4. (*a*) Schematics of constructs. (*Gray*, head of native myosin VI; *green* (C), converter domain; *purple* (UI), calmodulin binding unique insert; *cyan* (IQ), IQ domain; *orange* (PT), proximal tail domain; *red* (MT), medial tail domain; *brown* (G), GCN4; *yellow*, HaloTag; *blue* (2R), two spectrin repeats from α-actinin; and *wavy line*, $(GSG)_3$ flexible linkers.) (*b*) Cartoon of M6-GCN4 structure, color-coded to match part *a*. (*c*) Example stepping traces for M6-GCN4 (*red*) and M6DI$_{816}$-2R~MT-GCN4 (*blue*). Steps fit to these traces (*black*). (*d*) Distributions of stride sizes for M6-GCN4 and M6DI$_{816}$-2R~MT-GCN4. Stride size histograms (*markers*) are shown with a fit to the distribution of positive stride sizes (*solid*). Error bars are calculated as the square-root of the number of strides in each bin, scaled to proportion of strides. Peak positive stride sizes are 33.5 $\pm$ 0.7 nm (N = 158) for M6-GCN4 (*red*) and 30.1 $\pm$ 0.6 nm (N = 252) for M6DI$_{816}$-2R-MT-GCN4 (*blue*). (*e*) Dwell-time distributions for M6-GCN4 (*red*), mean dwell-time of 8.7 $\pm$ 0.7 s and M6DI$_{816}$-2R~MT-GCN4 (*blue*), mean dwell-time of 7.4 $\pm$ 0.4 s. Short dwells below a cutoff (*dashed lines*) were ignored to avoid undersampling near our time resolution. Curves (*solid black*) are exponential distributions with decay constants equal to the mean dwell-time, shifted by the undersampling cutoff.

We first describe a two-state, conceptual model, followed by the three-state model we used to perform fits.

The simplest model includes only two states for each head: bound to or detached from the actin filament. There are two different effects that can break symmetry in a two-headed walker (35):

1. It can be more likely for the rear head to detach than for the front head.
2. A released head can preferentially bind in front of, rather than behind, the remaining attached head.

Either of these effects is sufficient on its own to ensure directional motion. We assume that the second effect always occurs for myosin VI. It is the first effect that we describe here as "gating"; thus "perfect gating" means that the front head never detaches.

In this simple scheme, it is clear that a high duty ratio can result in significant processivity, as has been suggested (11). The probability of the dimer detaching during any cycle (meaning the second head detaches during the period of the cycle that the first head is already detached) is $1-r$, where r corresponds to the duty ratio of a monomeric motor, and is given by the rebinding rate over the sum of the rebinding and detachment rates. The average number of ATP cycles (equivalent to head detachment/reattachment cycles) carried out by the motor before completely dissociating is $r/(1-r)$. (See Note in the Supporting Material.) This also represents the average number of forward strides in the presence of perfect gating. However, statistically half of these cycles would be unproductive in the absence of gating, yielding an observed run-length of $r/(2*(1-r)$.) Thus, perfect gating only increases the run-length twofold in this model, while at high duty ratios run-length is inversely proportional to the percentage of the cycle spent detached ($1-r$).

Though this two-state model is instructive, and we expect its trends to carry through to more complicated models, its simplicity prevents it from differentiating among types of gating mechanisms. We therefore used a model with three states: bound to both actin filament and ADP; bound to the actin filament while not bound to nucleotide; and detached from the actin filament while bound to ATP (see Fig. 2, *a* and *b*, and Materials and Methods). Transfers between states are irreversible (as we assume the reverse rates are slow enough to be ignored) and we assume the free head always rebinds in front of the attached head, guaranteeing unidirectional travel. Three rate constants are needed to describe this model: the actomyosin ADP release rate, the apparent actomyosin ATP binding rate, and the actin-rebinding rate of the detached head.

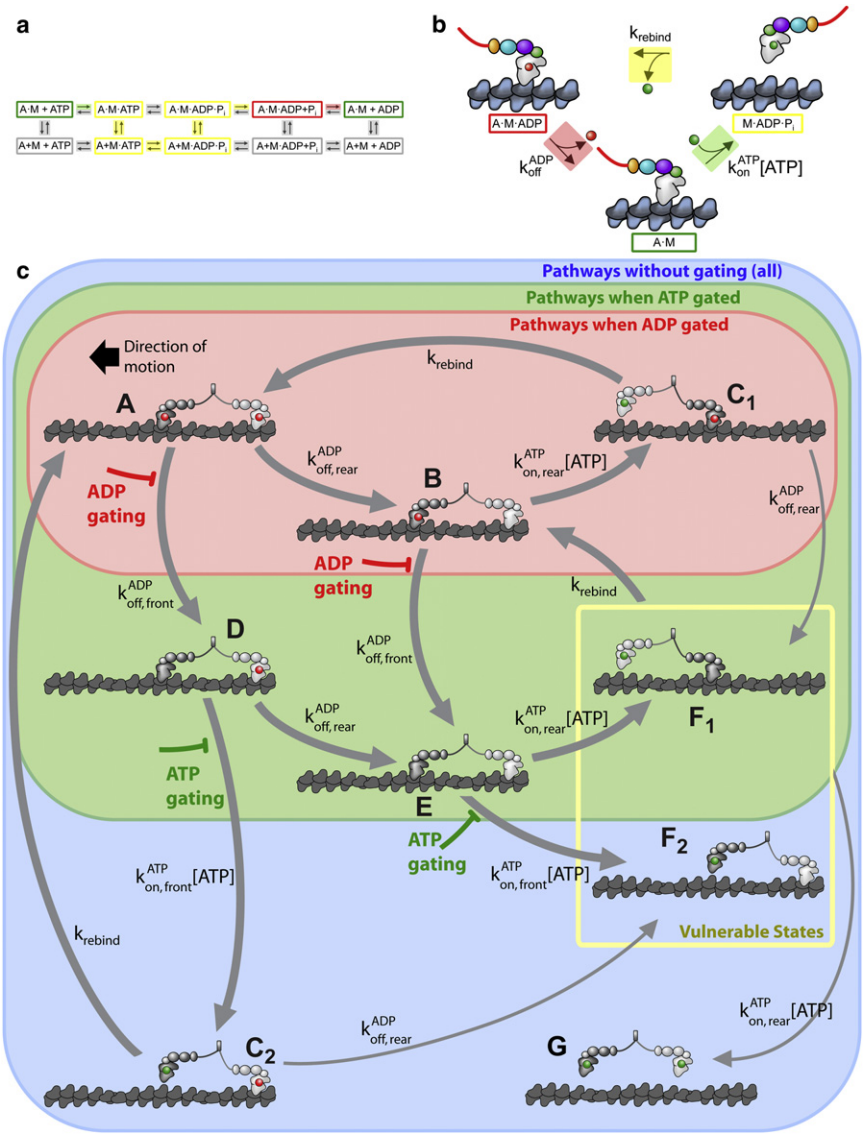

FIGURE 2 Three-state model for myosin VI kinetic cycle. (*a*) Schematic of kinetic pathway (based on de la Cruz et al. (5)) showing which states are grouped together or ignored in the simplified kinetic model. (*Green*) States in which myosin is bound to actin in the absence of nucleotide. (*Yellow*) States in which myosin is detached or weakly bound to the actin filament. (*Red*) States in which myosin is bound to actin and ADP. The remaining states (*gray*) are assumed to have negligible contributions. (*b*) Cartoon of the modeled kinetic cycle of a single myosin head. States and transitions between states are colored to match panel *a*. The prestroke state (*yellow box*) is bound to ADP.P_i (*green circle*) and unbound from actin. At rate k_{rebind}, myosin rebinds to actin, releases phosphate, and strokes, bringing it to a poststroke state (*red box*) where it is bound to actin and ADP (*red circle*). Note that k_{rebind} may actually be limited by phosphate release or the weak to strong transition instead of rebinding. ADP is released at rate k^{ADP}_{off} to enter a state where the motor is in a poststroke conformation and bound to actin but not nucleotide (*green box*). The cycle is completed when myosin binds ATP at rate k^{ATP}_{on} and releases from the actin filament. (*c*) Diagram of transitions in a dimeric motor, highlighting the paths that predominate with different mechanisms of gating. Motor begins in state A, and forward steps are directed toward the left (*black arrow*). Myosin heads are marked as containing ATP or ADP.P_i (*green dot*), ADP (*red dot*), or no nucleotide (*no dot*) at the nucleotide binding site. Transitions that are in competition with rebinding (*thinner arrows*) have low probabilities because the rebinding rate is the fastest rate in the cycle. Shading indicates the predominant pathways in the case of gating of ADP release (*pink*); in the case of gating of ATP binding (*green shading, which includes the pink shaded region*); and in the case of no gating (*blue shading, which encompasses all states*). Inhibition marks indicate rates that are slowed by gating of ADP release (*red*) or gating of ATP binding (*green*).

This three-state model for each head can be used as the foundation for a dimeric model by allowing each head to cycle through these three states independently, creating a branched kinetic pathway with a total of nine states (Fig. 2 *c*). Which pathways of this model are predominantly visited depends on the mechanism of gating. If ADP release is gated, myosin VI predominantly visits a pathway through states A, B, and C_1 (*shaded pink*) because transitions from A→D and from B→E are inhibited by the slowed ADP release rate from the front head. If binding of ATP is gated, but release of ADP is not, myosin VI will predominantly follow the green-shaded pathways (which include the *pink-shaded area*) because D→C2 and E→F2 transitions are inhibited by the slowed front head ATP binding rate. In the absence of gating, all pathways (*shaded blue*) are possible.

A total of five parameters are possible in the model described thus far because the ADP release rates and apparent ATP binding rates may be different between the front and rear heads. However, to assess the effects of gating mechanisms, for each fit we set the ratio of ADP release rates and the ratio of ATP binding rates to be fixed constants (which varied depending on the gating mechanism), reducing the number of parameters to three. Additionally, a fourth parameter was added to account for runs that terminate prematurely due to actin filament effects, such as defects in the actin filaments or their interactions with the coverslip (as described below).

Assuming that a productive step occurs when the rear head detaches while the front head remains attached and strokes, and that a run terminates when both heads detach simultaneously, we used this model to derive analytic

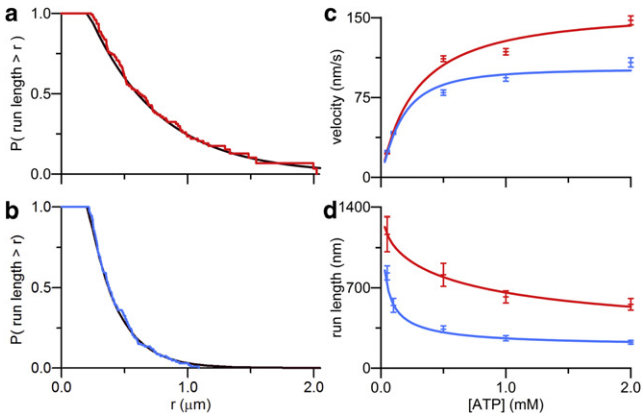

FIGURE 3 Velocity and run-length measurements for M6-GCN4 and M6DI$_{816}$-2R~MT-GCN4. (*a*) M6-GCN4 (*red*) and (*b*) M6DI$_{816}$-2R~MT-GCN4 (*blue*) at 2 mM ATP. Kaplan-Meier survivor functions, with compensation for runs terminating at filament ends (32,33), are shown (*color*). Exponential distributions based on the Kaplan-Meier estimate of the mean (0.556 ± 0.050 μm for M6-GCN4; 0.226 ± 0.016 μm for M6DI$_{816}$-2R~MT-GCN4) are shown (*solid black*). Runs shorter than 0.216 μm (two pixels) are truncated due to undersampling of runs close to our time resolution, and the mean estimator has been shifted accordingly (see Materials and Methods). (*c*) Velocity and (*d*) run-length as a function of ATP concentration for M6-GCN4 (*red*) and M6DI$_{816}$-2R~MT-GCN4 (*blue*). M6DI$_{816}$-2R~MT-GCN4 is slightly slower than M6-GCN4. If velocities for both constructs are scaled to an expected stepping rate (based on measured stepsize), the velocity difference is reduced, because the chimera has a slightly shorter stepsize (Fig. S7). M6DI$_{816}$-2R~MT-GCN4 shows reduced processivity compared to M6-GCN4, possibly as a result of damaged gating. (*Error bars*) Standard deviation of bootstrapped mean (for velocity) and Kaplan Meier estimate for standard deviation of the mean (run-length). (*Solid lines*) Fit to processivity model (see parameters in Table 1).

expressions for average run-length and velocity as a function of ATP concentration, effective ATP binding rates to the front and rear heads, ADP release rates from the front and rear heads, actin rebinding rate of the detached head, and actin defect parameter (see Note in the Supporting Material). These expressions were derived by summing over all possible pathways toward a productive step or dissociation (see Fig. 2 *c*, Fig. S4 and Fig. S5, and Note in the Supporting Material). These summations were calculated in a manner similar to that discussed in Ninio (36) by considering the relative probabilities of transitions at each branch point, were verified by Monte Carlo simulation (Fig. S3), and are derived in detail in the Supporting Material. Gating mechanisms were incorporated into the model by varying the ratio of front/rear head ATP binding rates or front/rear head ADP release rates.

Comparison of modeled and measured processivity

We measured average velocities and run-lengths, correcting for the finite length of the actin filaments, across a range of ATP concentrations (Fig. 3 and Materials and Methods). Both M6DI$_{816}$-2R~MT-GCN4 and M6-GCN4 exhibited similar velocities as a function of ATP concentration. Both constructs showed increased run-lengths at lower concentrations of ATP, as expected because the duty ratio is increased when ATP-binding is rate-limiting.

We first fit our processivity and velocity data for M6-GCN4 to the model assuming 10-fold gating of ADP release (that is, slowing the release of ADP from the front head by a factor of 10 when both heads are attached). This has recently been proposed as a lower bound on ADP release gating, based on high time-resolution, single-molecule myosin VI measurements (15). This model fits quantitatively to our data (Fig. 3, *c* and *d*, and Table 1), and yields parameters in good agreement with previously published values based on bulk kinetic measurements (5,16).

Although the chimera M6DI$_{816}$-2R~MT-GCN4 is highly processive, it is less processive than M6-GCN4 (Fig. 3 *d*). One explanation is that gating is damaged in this construct because the forces transmitted between the heads are altered by the artificial lever arm. This is likely because the flexible

TABLE 1 Modeling parameters for fits/models shown in Figs. 3 and 4

Construct	$k^{ADP}_{off,rear}$ (s^{-1})	$k^{ATP}_{on,rear}$ ($\mu M^{-1}\ s^{-1}$)	k_{rebind} (s^{-1})	$k^{ADP}_{off,front}$ (s^{-1})	$k^{ATP}_{on,front}$ ($\mu M^{-1}\ s^{-1}$)	Steps per actin defect
M6-GCN4	**5.1 ± 0.2***	**0.016 ± 0.001***	**57 ± 12***	0.5	0.016	**48 ± 11***
M6DI$_{816}$-2R~MT-GCN4	**3.8 ± 0.1***	0.016	57	3.8	0.016	48
ADP-release gating model	5.1	0.016	57	0.5	0.016	48
ATP-binding gating model	5.1	0.016	57	5	0.0016	48
No gating model	5.1	0.016	57	5	0.016	48
Relevant previous measurements	5.6[†]	0.018[†]	89[†,¶]			
	5.3[‡]	0.03[‡,§]	28.2[‡,‖]			

Parameters marked in bold were allowed to vary independently in the fits. The front head ADP release and ATP binding rates were varied with fixed ratios to the rear head rates; all other parameters not in bold were fixed. Error estimates were generated using parametric bootstrapping (see Materials and Methods in this article, and Methods in the Supporting Material).

*Parameters allowed to vary independently in fits.

[†]From de la Cruz et al. (5).

[‡]From Sweeney et al. (16).

[§]Strong-to-weak transition.

[¶]P_i release rate.

[‖]Weak-to-strong transition.

linker between the artificial lever arm and medial tail should serve to reduce tension that might otherwise be transmitted between the heads. The velocity data for the chimera are slower at high concentrations of ATP, when ADP release is rate-limiting, but not at low concentrations of ATP, when ATP binding is rate-limiting, suggesting that the rate of ADP release is somewhat slowed in the chimera whereas the rate of ATP binding remains the same (Fig. 3 *c*).

To test consistency with our model, we fit a new ADP release rate to the M6DI$_{816}$-2R~MT-GCN4 velocity data and otherwise used the same parameters from the M6-GCN4 fit described above, but removed gating by setting the front and rear head ADP release rates equal. The theory agrees with the processivity and velocity data for this construct, using only a one-parameter fit to the velocity and a zero-parameter fit to the processivity (Fig. 3, *c* and *d*, Table 1). Although the gating mechanisms we have described (10-fold slowing of ADP release to the front head in M6-GCN4 and no gating in M6DI$_{816}$-2R~MT-GCN4) are consistent with our processivity data, other interpretations are also consistent with this type of modeling. For instance, it would be possible to fit the chimera processivity data by altering all four modeling parameters and including some gating, or to fit the M6-GCN4 data without gating. However, these fits require more free parameters than the fit we have shown, yield parameters with less consistency between constructs, and give rebinding rates that are less consistent with previously measured values (Fig. S6 and Table S1).

Surface attachment effects on processivity

Processivity in both constructs was affected by the mechanism of attachment of actin filaments to the coverslip. When we used a higher concentration of NEM-treated HMM (see Materials and Methods) to attach actin to the surface, we observed shorter runs, suggesting that myosin bumping into an attachment point more frequently increases the frequency of run termination (Table S2). We also found that biotinylating actin to attach it to the surface, likely a less flexible attachment mechanism than NEM-HMM, shortened the runs (data not shown). These effects led us to add an additional actin defect parameter to our modeling, and we found that it varied between batches of actin filaments or NEM-HMM (see Table 1 and Table S3). Because these results showed that the state of the actin binding to the surface affects the run-length, we collected all directly-compared processivity data (e.g., all data in Fig. 3 and, separately, all data in Fig. S8) using single batches of actin and the minimum amount of NEM-HMM necessary to attach actin.

Effect of free Mg^{2+} on processivity

As a further demonstration of the effectiveness of the model, we used it to make predictions of the effect on processivity of altering free Mg^{2+} concentration. Free Mg^{2+} concentration can alter the velocity (37,38) and processivity (25,39) of a molecular motor. Therefore, we compensated for changes in the ATP concentration to keep the amount of free Mg^{2+} constant in the experiments described above (see Materials and Methods). It has been observed for myosin V and myosin I that the ADP release rate is dependent on the Mg^{2+} concentration, with the suggested mechanism that Mg^{2+} must release from the nucleotide binding pocket before ADP (37–39). We observe a similar effect in myosin VI: at high ATP concentrations, when ADP release is rate-limiting, higher Mg^{2+} concentrations result in slower velocities (Fig. S8 *a*).

Assuming free Mg^{2+} affects only ADP-release, we fit that parameter to each point in the velocity data, and used our model to predict the corresponding expected run-length (with the additional actin binding parameter fit as well across all Mg^{2+} concentrations) (Fig. S8 and Table S3). This predicts that higher Mg^{2+} concentrations and slower velocities should cause a corresponding increase in processivity, as we observe.

Effects of gating mechanisms on processivity

After creating and testing a kinetic model (see Fig. 2 *c* and Note in the Supporting Material) for myosin VI stepping, we used the model to better understand how gating should be expected to affect processivity. We fixed the modeling parameters to the values described in the earlier fit to M6-GCN4, and calculated processivities resulting from different gating mechanisms. We compared three possibilities: no gating (each head cycles independently); 10-fold slowing of ADP release from the front head; and 10-fold slowing of ATP binding to the front head (Fig. 4). Clearly, effective processivity is possible in the absence of intramolecular gating. In fact, if we look at the most physiologically

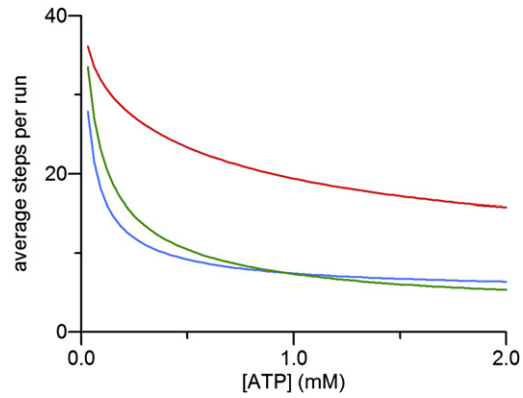

FIGURE 4 Comparison of processivity model using different mechanisms of gating: no gating (*blue*), 10-fold gating of ADP release from front head (*red*), and 10-fold gating of ATP binding to front head (*green*). Parameters input into this model are the same as the M6-GCN4 fit shown in Fig. 3. All parameters are kept constant when comparing the models; only the mechanism of gating is changed (see Table 1).

relevant region of this curve, at the highest ATP concentrations, we find that gating of ADP release only improves processivity by approximately a factor of 2.5, and that, perhaps surprisingly, gating of ATP binding slightly decreases processivity.

The potential for ATP gating to disrupt processivity can be understood by considering what happens when the front head releases ADP before the rear head and the motor enters state D (Fig. 2 *c*). This event occurs frequently unless ADP release is gated. At high ATP concentration in the absence of any gating, the front head will usually rebind ATP and regenerate state A via a pathway (D→C2→A) that wastes an ATP hydrolysis but is relatively safe from dissociation because the one-head bound state (C2) has ADP bound. However, ATP gating specifically inhibits this pathway, and thus the motor proceeds through the only available alternative pathway, through state E to the very vulnerable state F (Fig. 2 *c*, *yellow box*).

At low ATP concentrations, D→C2 becomes unlikely and the motor always proceeds through states E and F. Under these conditions, ATP gating is preferable to no gating because the motor proceeds through the productive state F1 rather than the unproductive state F2. There must thus be a crossover ATP concentration at which the protective effect of ATP rebinding to the front head fully compensates for the detrimental effect of unproductive cycling, as shown in Fig. 4.

Structural requirements for myosin VI processivity

We created two additional chimeras to further test the structural robustness of myosin VI processivity. These constructs are: M6PI$_{790}$-2R~MT-GCN4, identical to the previous chimera except that the distal, calmodulin-binding portion of the unique insert has been removed, and the artificial lever arm is fused after the proximal portion of the unique insert, which redirects the lever arm; and M6DI$_{816}$-2R~GCN4$_{IL}$, identical to the first chimera except that the medial tail has been removed and a hyperstable mutant of GCN4 (40) immediately follows the swivel (Fig. 5 *a*). (We were not able to demonstrate processivity in a M6DI$_{816}$-2R~GCN4 construct with GCN4 alone.)

Results with these constructs demonstrate that myosin VI processivity is possible without the medial tail and in the absence of calmodulin (see Fig. 5, and Movie S3 and Movie S4). Removal of the unique insert calmodulin is a dramatic structural modification, considering the close interaction of this calmodulin with the converter domain (6,41). All three chimeric structures show remarkable similarity in their basic behavior to our M6-GCN4 control: they are able to take multiple steps along the actin filament without detaching, with similar stride sizes and kinetics (Fig. 5, *b–d*). All three chimeras do have slightly shorter stride sizes than M6-GCN4, showing that processivity is

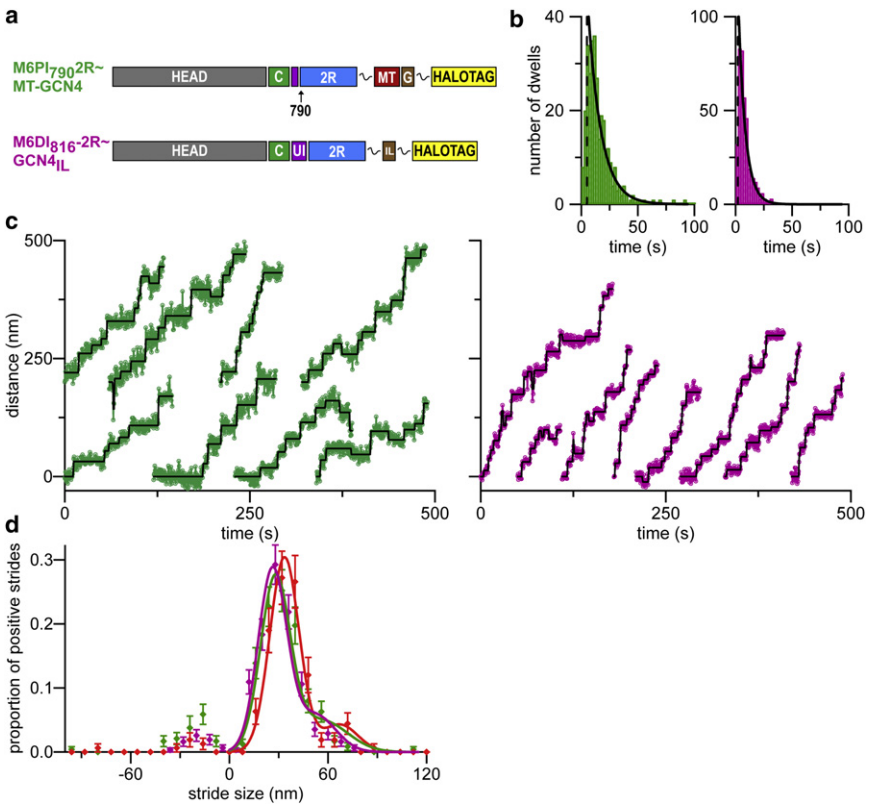

FIGURE 5 Single molecule stepping results for M6PI$_{790}$-2R~MT-GCN4 and M6DI$_{816}$-2R~GCN4$_{IL}$ at 5 μM ATP. (*a*) Schematic of constructs. (*Gray*, head of native myosin VI; *green* (*C*), converter domain; *purple* (UI), calmodulin binding unique insert or unique insert truncated at residue 790 (before calmodulin binding site); *red* (MT), medial tail domain; *brown* (G/IL), GCN4 or GCN4$_{IL}$; *yellow*, HaloTag; *blue* (2R), two spectrin repeats from α-actinin; and *wavy line*, (GSG)$_3$ flexible linkers.) (*b*) Dwell-time distributions at 5 μM ATP for M6PI$_{790}$-2R~MT-GCN4 (*green*), mean dwell-time of 11.7 $\pm$ 0.7 s and M6DI$_{816}$-2R~GCN4$_{IL}$ (*magenta*), mean dwell-time of 6.3 $\pm$ 0.3 s. (*Dotted lines*) Cutoff of short dwells from undersampling near our time resolution. Curves (*solid black*) are exponential distributions with time constants of the mean dwells, shifted by the undersampling cutoff. (*c*) Example stepping traces of M6PI$_{790}$-2R~MT-GCN4 (*green*) and M6DI$_{816}$-2R~GCN4$_{IL}$ (*magenta*). Modeled steps are shown (*black*). (*d*) Stride size distributions of chimeras with M6-GCN4 for comparison. Histograms are shown with fits as in Fig. 1. Peak positive stride sizes are 33.5 $\pm$ 0.7 nm (N = 158) for M6-GCN4 (*red*), 27.9 $\pm$ 0.6 nm (N = 238) for M6PI$_{790}$-2R~MT-GCN4 (*green*), and 26.2 $\pm$ 0.5 nm (N = 335) for M6DI$_{816}$-2R~GCN4$_{IL}$ (*magenta*).

possible even when the stride size does not match the actin pseudorepeat, as seen for mutant versions of myosin V (25,42,43).

Processivity is readily observable over the full range of ATP concentrations for both M6DI$_{816}$-2R constructs and for the control M6-GCN4 dimer. M6PI$_{790}$-2R~MT-GCN4, the sole construct lacking calmodulin, is minimally processive and requires very low ATP concentration for processivity to be observed. This construct also shows a change in kinetics, with its dwell-time increased by almost a factor of two (at low ATP concentrations), and it takes backward steps more frequently than the other chimeras and the control dimer (Fig. 5, *b* and *d*). It also appears to lose activity (as observed by a loss of processive motion) more quickly after being prepared than the other constructs. The unique insert/converter regions, which interact with calmodulin in the native structure, may be less stable in the absence of these interactions.

DISCUSSION

Processivity is an ability that the myosin VI dimer shares with several other myosins, and with molecular motors such as kinesin and dynein. We have assessed features that might be important for achieving processivity, such as appropriate stride size, high duty ratio, and intramolecular gating. Myosins V and VI and kinesin-1 have each been demonstrated to exhibit a gating mechanism that keeps the kinetic cycles of the two heads out of phase (5,13,44,45). It has been proposed (11,16) that one purpose of this gating is to increase processivity by preventing both heads from detaching from the actin filament or microtubule simultaneously. However, gating is not strictly required for processivity (11,24).

We created three chimeric constructs with a variety of changes engineered into the myosin VI lever arm, including replacement of the medial tail, proximal tail, IQ domain, and calmodulin-binding unique insert, which interacts closely with the converter domain. Despite these significant changes, all three chimeric constructs exhibit similar behavior to M6-GCN4 verifying that either:

1. Gating is extremely robust to changes in the physical properties of the lever arm, including portions that interact with the converter domain.
2. Gating is not necessary for processivity.

By comparing measured processivity and modeling, we demonstrate that a high degree of processivity is to be expected even in the absence of gating, as long as there is a sufficiently high duty ratio, and that gating does not necessarily increase processivity. This is supported by a recent finding that a myosin V construct with a single α-helix domain replacing the native lever arm is processive but does not exhibit gating (24).

Because gating does exist in myosin VI (5), it is worth considering possible physical origins and biological functions for this effect. Differences in kinetics between the front and rear heads might be expected to arise even in the absence of evolutionary selection for this effect, as a consequence of coupling between the lever arm and nucleotide binding pocket. Although we have shown that gating does not necessarily increase processivity, it does improve the efficiency of the motor by preventing the wasting of ATP on unproductive cycles. Additionally, gating may prevent backward motion under load (46). Gating mechanisms prevent the front head from releasing from the actin filament. If the front head detaches under load, it can cause the motor to take a backward step (47). Prevention of front head detachment could be critical for known roles of myosin VI as a cargo transporter and cytoskeletal anchor.

Finally, the possibility of creating highly artificial and yet processive dimers raises questions about the in vivo relevance of previous measurements on forced dimers. When the M6-GCN4 construct, and other similar control dimers (3,4,15,48–51) were created, it was assumed the medial tail formed a coiled-coil (4), so GCN4 was expected to reinforce, not provide, dimerization. It is now known that full-length myosin VI is monomeric in solution (52), but may become dimeric when bound to cargo (53). The similarity of M6-GCN4 to myosin V, which forms a dimer in vivo, might have been interpreted as evidence that this control dimer recapitulates the in vivo configuration of myosin VI. However, the very similar behavior of our dramatically altered chimeras suggests that caution is warranted in assuming that processive ~36-nm steps must reflect evolutionarily selected behavior.

SUPPORTING MATERIAL

Eight figures, three tables, four movies, and 42 equations with additional methods and a note are available at http://www.biophysj.org/biophysj/supplemental/S0006-3495(10)01444-X.

We thank R. Cooke and K. Franks-Skiba for a gift of HMM, S. Sutton for technical assistance, A. Dunn, P. Chuan, S. Sivaramakrishnan, and J. M. Sung for helpful discussions, and P. Shaklee, J. Mercer, R. Das, A. Karunakaran, K. Frieda, and M. Larson for comments on the manuscript.

This work was supported by National Institutes of Health grant No. GM33289 and Human Frontier Science Program grant No. RGP054/2009-C to J.A.S. and National Institutes of Health grant No. DP2 OD004690 to Z.B. M.W.E. was supported by a National Science Foundation Graduate Research Fellowship and an Achievement Rewards for College Scientists (ARCS) Foundation Scholarship.

REFERENCES

1. Sweeney, H. L., and A. Houdusse. 2007. What can myosin VI do in cells? *Curr. Opin. Cell Biol.* 19:57–66.

2. Spudich, J. A., and S. Sivaramakrishnan. 2010. Myosin VI: an innovative motor that challenged the swinging lever arm hypothesis. *Nat. Rev. Mol. Cell Biol.* 11:128–137.
3. Okten, Z., L. S. Churchman, …, J. A. Spudich. 2004. Myosin VI walks hand-over-hand along actin. *Nat. Struct. Mol. Biol.* 11:884–887.
4. Rock, R. S., S. E. Rice, …, H. L. Sweeney. 2001. Myosin VI is a processive motor with a large step size. *Proc. Natl. Acad. Sci. USA.* 98:13655–13659.
5. de la Cruz, E. M., E. M. Ostap, and H. L. Sweeney. 2001. Kinetic mechanism and regulation of myosin VI. *J. Biol. Chem.* 276:32373–32381.
6. Ménétrey, J., A. Bahloul, …, A. Houdusse. 2005. The structure of the myosin VI motor reveals the mechanism of directionality reversal. *Nature.* 435:779–785.
7. Bryant, Z., D. Altman, and J. A. Spudich. 2007. The power stroke of myosin VI and the basis of reverse directionality. *Proc. Natl. Acad. Sci. USA.* 104:772–777.
8. Park, H., A. Li, …, H. L. Sweeney. 2007. The unique insert at the end of the myosin VI motor is the sole determinant of directionality. *Proc. Natl. Acad. Sci. USA.* 104:778–783.
9. Bahloul, A., G. Chevreux, …, H. L. Sweeney. 2004. The unique insert in myosin VI is a structural calcium-calmodulin binding site. *Proc. Natl. Acad. Sci. USA.* 101:4787–4792.
10. Spink, B. J., S. Sivaramakrishnan, …, J. A. Spudich. 2008. Long single α-helical tail domains bridge the gap between structure and function of myosin VI. *Nat. Struct. Mol. Biol.* 15:591–597.
11. Veigel, C., F. Wang, …, J. E. Molloy. 2002. The gated gait of the processive molecular motor, myosin V. *Nat. Cell Biol.* 4:59–65.
12. Robblee, J. P., A. O. Olivares, and E. M. de la Cruz. 2004. Mechanism of nucleotide binding to actomyosin VI: evidence for allosteric head-head communication. *J. Biol. Chem.* 279:38608–38617.
13. Rief, M., R. S. Rock, …, J. A. Spudich. 2000. Myosin-V stepping kinetics: a molecular model for processivity. *Proc. Natl. Acad. Sci. USA.* 97:9482–9486.
14. Oguchi, Y., S. V. Mikhailenko, …, S. Ishiwata. 2008. Load-dependent ADP binding to myosins V and VI: implications for subunit coordination and function. *Proc. Natl. Acad. Sci. USA.* 105:7714–7719.
15. Dunn, A. R., P. Chuan, …, J. A. Spudich. 2010. Contribution of the myosin VI tail domain to processive stepping and intramolecular tension sensing. *Proc. Natl. Acad. Sci. USA.* 107:7746–7750.
16. Sweeney, H. L., H. Park, …, S. S. Rosenfeld. 2007. How myosin VI coordinates its heads during processive movement. *EMBO J.* 26:2682–2692.
17. Sweeney, H. L., and A. Houdusse. 2010. Myosin VI rewrites the rules for myosin motors. *Cell.* 141:573–582.
18. Lan, G., and S. X. Sun. 2005. Dynamics of myosin-V processivity. *Biophys. J.* 88:999–1008.
19. Vilfan, A. 2005. Elastic lever-arm model for myosin V. *Biophys. J.* 88:3792–3805.
20. Anson, M., M. A. Geeves, …, D. J. Manstein. 1996. Myosin motors with artificial lever arms. *EMBO J.* 15:6069–6074.
21. Liao, J. C., M. W. Elting, …, Z. Bryant. 2009. Engineered myosin VI motors reveal minimal structural determinants of directionality and processivity. *J. Mol. Biol.* 392:862–867.
22. Manstein, D. J. 2004. Molecular engineering of myosin. *Philos. Trans. R. Soc. Lond. B Biol. Sci.* 359:1907–1912.
23. Homma, K., M. Yoshimura, …, M. Ikebe. 2001. The core of the motor domain determines the direction of myosin movement. *Nature.* 412:831–834.
24. Baboolal, T. G., T. Sakamoto, …, M. Peckham. 2009. The SAH domain extends the functional length of the myosin lever. *Proc. Natl. Acad. Sci. USA.* 106:22193–22198.
25. Amrute-Nayak, M., R. P. Diensthuber, …, G. Tsiavaliaris. 2010. Targeted optimization of a protein nanomachine for operation in biohybrid devices. *Angew. Chem. Int. Ed. Engl.* 49:312–316.
26. Thorn, K. S., J. A. Ubersax, and R. D. Vale. 2000. Engineering the processive run length of the kinesin motor. *J. Cell Biol.* 151:1093–1100.
27. Yildiz, A., M. Tomishige, …, R. D. Vale. 2008. Intramolecular strain coordinates kinesin stepping behavior along microtubules. *Cell.* 134:1030–1041.
28. Adio, S., J. Jaud, …, G. Woehlke. 2009. Dissection of kinesin's processivity. *PLoS ONE.* 4:e4612.
29. Miyazono, Y., M. Hayashi, …, H. Tadakuma. 2010. Strain through the neck linker ensures processive runs: a DNA-kinesin hybrid nanomachine study. *EMBO J.* 29:93–106.
30. Yildiz, A., J. N. Forkey, …, P. R. Selvin. 2003. Myosin V walks hand-over-hand: single fluorophore imaging with 1.5-nm localization. *Science.* 300:2061–2065.
31. Kerssemakers, J. W., E. L. Munteanu, …, M. Dogterom. 2006. Assembly dynamics of microtubules at molecular resolution. *Nature.* 442:709–712.
32. Kaplan, E. L., and P. Meier. 1958. Nonparametric estimation from incomplete observations. *J. Am. Stat. Assoc.* 53:457–481.
33. Nagy, S., B. L. Ricca, …, R. S. Rock. 2008. A myosin motor that selects bundled actin for motility. *Proc. Natl. Acad. Sci. USA.* 105:9616–9620.
34. Baker, J. E., E. B. Krementsova, …, D. M. Warshaw. 2004. Myosin V processivity: multiple kinetic pathways for head-to-head coordination. *Proc. Natl. Acad. Sci. USA.* 101:5542–5546.
35. Astumian, R. D. 2010. Thermodynamics and kinetics of molecular motors. *Biophys. J.* 98:2401–2409.
36. Ninio, J. 1987. Alternative to the steady-state method: derivation of reaction rates from first-passage times and pathway probabilities. *Proc. Natl. Acad. Sci. USA.* 84:663–667.
37. Fujita-Becker, S., U. Dürrwang, …, D. J. Manstein. 2005. Changes in Mg^{2+} ion concentration and heavy chain phosphorylation regulate the motor activity of a class I myosin. *J. Biol. Chem.* 280:6064–6071.
38. Rosenfeld, S. S., A. Houdusse, and H. L. Sweeney. 2005. Magnesium regulates ADP dissociation from myosin V. *J. Biol. Chem.* 280:6072–6079.
39. Taft, M. H., F. K. Hartmann, …, G. Tsiavaliaris. 2008. *Dictyostelium* myosin-5b is a conditional processive motor. *J. Biol. Chem.* 283:26902–26910.
40. Harbury, P. B., T. Zhang, …, T. Alber. 1993. A switch between two-, three-, and four-stranded coiled coils in GCN4 leucine zipper mutants. *Science.* 262:1401–1407.
41. Ménétrey, J., P. Llinas, …, A. Houdusse. 2008. The post-rigor structure of myosin VI and implications for the recovery stroke. *EMBO J.* 27:244–252.
42. Purcell, T. J., C. Morris, …, H. L. Sweeney. 2002. Role of the lever arm in the processive stepping of myosin V. *Proc. Natl. Acad. Sci. USA.* 99:14159–14164.
43. Sakamoto, T., A. Yildez, …, J. R. Sellers. 2005. Step-size is determined by neck length in myosin V. *Biochemistry.* 44:16203–16210.
44. Sakamoto, T., M. R. Webb, …, J. R. Sellers. 2008. Direct observation of the mechanochemical coupling in myosin Va during processive movement. *Nature.* 455:128–132.
45. Block, S. M. 2007. Kinesin motor mechanics: binding, stepping, tracking, gating, and limping. *Biophys. J.* 92:2986–2995.
46. Uemura, S., H. Higuchi, …, S. Ishiwata. 2004. Mechanochemical coupling of two substeps in a single myosin V motor. *Nat. Struct. Mol. Biol.* 11:877–883.
47. Gebhardt, J. C., A. E. Clemen, …, M. Rief. 2006. Myosin-V is a mechanical ratchet. *Proc. Natl. Acad. Sci. USA.* 103:8680–8685.

48. Nishikawa, S., K. Homma, …, M. Ikebe. 2002. Class VI myosin moves processively along actin filaments backward with large steps. *Biochem. Biophys. Res. Commun.* 290:311–317.

49. Sun, Y., H. W. Schroeder, 3rd, …, Y. E. Goldman. 2007. Myosin VI walks "wiggly" on actin with large and variable tilting. *Mol. Cell.* 28:954–964.

50. Park, H., B. Ramamurthy, …, H. L. Sweeney. 2006. Full-length myosin VI dimerizes and moves processively along actin filaments upon monomer clustering. *Mol. Cell.* 21:331–336.

51. Mukherjea, M., P. Llinas, …, H. L. Sweeney. 2009. Myosin VI dimerization triggers an unfolding of a three-helix bundle in order to extend its reach. *Mol. Cell.* 35:305–315.

52. Lister, I., S. Schmitz, …, J. Kendrick-Jones. 2004. A monomeric myosin VI with a large working stroke. *EMBO J.* 23:1729–1738.

53. Phichith, D., M. Travaglia, …, H. L. Sweeney. 2009. Cargo binding induces dimerization of myosin VI. *Proc. Natl. Acad. Sci. USA.* 106:17320–17324.